The effects of defects on the uniaxial compressive strength and failure of an advanced ceramic

James David Hogan[a,b], Lukasz Farbaniec[b], Tomoko Sano[c], Matthew Shaeffer[b], K.T. Ramesh[b,d]

[a]*Department of Mechanical Engineering, The University of Alberta, Edmonton, AB T6G 2R3, Canada*
[b]*Hopkins Extreme Materials Institute, The Johns Hopkins University, Baltimore, MD 21218, USA*
[c]*Weapons and Materials Research Directorate, Army Research Laboratory, Aberdeen Proving Grounds, MD 21005*
[d]*Department of Mechanical Engineering, The Johns Hopkins University, Baltimore, MD 21218, USA*

Abstract

This study investigates the effects of the processing-induced defect population on the dynamic compressive strength and failure of a hot-pressed boron carbide. Quantitative microscopic analysis was used to determine the distributions of three types of processing-induced inhomogeneities: aluminum nitride, small graphitic particles and pores, and larger graphitic disks. Scanning electron microscopy of fracture surfaces identifies the graphitic disks as fracture initiation sites. The size, orientation and number density of the graphitic disks are then quantified using image processing techniques. We use these defect statistics, in conjunction with recent scaling models, to explore our experimentally measured dynamic compressive strength results.

Keywords: compressive strength; defect statistics; brittle failure; experimental mechanics; microstructure design

Email address: jdhogan@ualberta.ca (James David Hogan)

1. Introduction

Designing new advanced ceramic materials for protective systems requires a fundamental understanding of high-rate failure mechanisms, and of the effects of microstructure on these mechanisms. The dynamic behavior of several advanced ceramics has been investigated (e.g., silicon carbide [1, 2], aluminum nitride [3], titanium diboride [4]) in terms of mechanisms such as dislocation activity [3], amorphization [5] and fracture and fragmentation [6]. In this study, we extend previous works on dynamic brittle failure in ceramics by investigating the links between the defect population and the uniaxial compressive strength and failure of a commercially available hot-pressed boron carbide.

The compressive failure of brittle materials is generally a result of the initiation, propagation and coalescence of cracks originating from defects (such as grain boundaries, inclusions, pre-existing micro-cracks and surface flaws). During quasi-static compression, a small number of relatively large flaws (or 'defects'- used interchangeably throughout) are activated and the resulting crack growth rate leads to rapid structural failure. During dynamic compression, the rate of loading is too large to be relaxed by crack growth of a few relatively large activated flaws. This results in the activation of additional, smaller defects, and this process also manifests as an increase in strength for increased rates [7–10].

The rate-sensitivity of the compressive strength of brittle materials has been shown to be strongly dependent on defect distributions [9, 11–13]. For example, a model developed by Paliwal and Ramesh [11] coupled the initial defect distribution, the dynamics of crack growth and crack-crack interactions, considering flaw size and flaw number density. Recent work by Hu et al. [12] extended this formulation to include anisotropic damage and the effect of flaw orientation on the dynamic failure of brittle materials.

Graham-Brady [13] extended the work of Paliwal and Ramesh [11] to include the effect of the localized flaw density on the dynamic compressive failure of brittle materials. More recently, Kimberley et al. [9] developed a scaling relation to describe the rate-dependent compressive strength of brittle materials that incorporates the interaction of a distribution of preexisting flaws and crack growth dynamics. Their analytical model was shown to provide reasonable agreement with simulation results using the Paliwal and Ramesh [11] model.

In this paper, we examine the links between the microstructure and the dynamic uniaxial compressive strength and failure of a hot-pressed boron carbide. We give particular attention to characterizing the defect populations (e.g., size, orientations and flaw density) and linking these with strength measurements. We then incorporate the defect statistics into the scaling relation developed by Kimberley et al. [9] to explore its applicability to boron carbide, including our hot-pressed material and a pressureless sintered material studied previously by Sano et al. [14].

2. Experimental Setup

Quasi-static and dynamic uniaxial compression experiments were performed on a hot-pressed boron carbide from Coorstek (Vista, California), with a Young's modulus of 430 GPa, a density of 2,510 kg/m^3, and a Poisson ratio of 0.16-0.17 (as determined by the manufacturer). The boron carbide material was received as tiles (conceptualized in Figure 1a) with dimensions of 305 mm in length, 254 mm in width, and 8 mm in thickness. Experiments were performed by loading sectioned specimens both parallel (termed "through-thickness": TT) and normal (termed "in-plane": IP) to the plate thickness, which is the hot-pressing direction (Figure 1a). The cuboidal specimens used in the compression tests were 5.3 mm in length, 3.5 mm in width and 4.0 mm in height.

These are conceptualized on the right in Figure 1a. The use of cuboidal specimens allows visualization of failure during dynamic loading.

Quasi-static uniaxial compression experiments were performed with an MTS servo-hydraulic test machine with a controlled displacement rate at a nominal strain rate of appoximately 10^{-4} s^{-1}. The dynamic uniaxial compression tests were performed using a modified Kolsky bar apparatus. Kolsky bar testing has been previously used to study the dynamic behavior of a variety of ceramic materials [1, 15–17], and experimental design is discussed therein. The nominal strain rates achieved in the dynamic tests were between 350 to 1,000 s^{-1}. The incident and transmitted bars were 12.7 mm in diameter and made of maraging steel (VascoMax C-350) with a yield strength of 2.68 GPa, a Young's modulus of 200 GPa, a Poisson's ratio of 0.29 and a density of 8,100 kg/m^3. Impedance-matched tungsten carbide platens were jacketed by Ti-6Al-4V alloy sleeves, and were inserted between the sample and the bars to act as a buffer and protect against sample indentation. A small amount of high-vacuum grease was applied to the end faces of both platens and specimen to reduce friction resulting from the mismatched Poisson ratio. A Kirana high-speed video camera filming at 5 Mfps with a 500 ns exposure time was used to capture sample failure. A pulsed laser was used to illuminate the specimen surface. Output pulses from the camera were used to synchronize the camera images with the stress-time history recorded with the strain gauge on the transmitted bar.

2.1. Microstructural Characterization

The inclusions and defects in the microstructure were characterized using a Zeiss optical microscope with an AxioCam MRC camera and a TESCAN MIRA3 field emission Scanning Electron Microscope (SEM) equipped with a fully automated electron backscatter diffraction (EBSD) analysis system and Energy Dispersive Spectroscopy

(EDS) capabilities. The word ”defect” is used to denote a microstructural feature that may serve as a failure initiation site (examined later) and ”inclusion” to denote a feature that is not believed to contribute to failure (at least not under the stress-states studied here). The processing-induced inclusions and defects are most easily seen in optical microscope images such as those shown in Figure 1b and c. The image on the left is taken on the TT face, while the image on the right is taken on the IP face. Note the different scale bars. Large approximately circular dark features are observed in the TT images in Figure 1b. These have been confirmed as carbonaceous/graphitic in composition with EDS measurements. Also highlighted in Figure 1b are smaller and more circular features. These are primarily smaller graphitic defects, with other smaller features consisting of cavities/pores (confirmed with SEM/EDS). Brighter phases are also noted in Figure 1b which appear to be primarily comprised of aluminum nitride (AlN) and boron nitride (BN) (confirmed with SEM/EDS). These inclusions are facetted structures less than 20 μm in size, and are commonly observed at boron carbide grain boundaries.

An image of the microstructure with normal in the in-plane (IP) direction is shown in Figure 1c (taken at 100$\times$ magnification). Larger elongated graphitic defects, smaller features (graphitic particles and pores) and the brighter AlN and BN phase are observed. Using the images in Figures 1b and 1c, we conclude that the mesoscale features are: larger disk-like graphitic defects, smaller features that are primarily comprised of graphitic, and AlN and BN inclusions. For clarity, we show the preferred orientation of the graphitic disks in the conceptualized tile in Figure 1a.

The boron carbide grain structure is presented in the boron carbide grain morphology in the EBSD map in Figure 2. Prior to EBSD, the sample was polished with diamond lapping films with grit sizes of less than 1 μm, and then ion-milled for 10 minutes at 3.5 kV. The resulting maps were analyzed with the OIM^{TM} software from EDAX

TexSem Laboratories (TSL). Boron carbide in the OIM^{TM} software was defined using a rhombohedral lattice system, R3$\bar{m}$ symmetry space group, with lattice constants (a = 0.5653 nm and c = 1.215 nm), as reported in Sologub et al. [18]. In addition, a validation procedure using single crystal boron carbide of known crystallographic orientations was used to ensure that the crystallographic orientation of grains was indexed properly. The inhomogeneities (i.e., possible secondary phases, inclusions or grain boundary films) were not the subject of interest in the EBSD analysis, therefore they are not indexed in the map in Figure 2. The mapping was performed in the IP direction with a step size of 0.2 μm.

The map shown in Figure 2 is a combined inverse pole figure (IPF), image quality (IQ) and grain-boundary maps of the hot-pressed boron carbide. Figure 2 shows that the structure consists of equiaxed grains with close to random crystallographic orientations. The measured average area-weighted grain sizes is approximately 5 μm (range of 4 to 10 μm in size). Almost all the grains are surrounded by boundaries with a high misorientation angle (>15°).

3. Experimental Results

In this section, links will be made between the defects and the strength and failure of a hot-pressed boron carbide. Dynamic uniaxial compressive strength measurements are presented, and some of the key types of defects governing failure are identified. Statistics of the defect size and orientation are then presented.

3.1. Uniaxial Dynamic Compressive Failure

Figure 3 shows a stress-time history curve (left) for a dynamic uniaxial compressive experiment together with time-resolved (1 to 4) high-speed camera images (right). The

material is being tested in the IP direction and imaged on the TT face. The loading and imaging orientations are shown as an inset in the stress-time plot. Highlighted in image 1 is the loading orientation, as well as an example of a near-circular black feature on the surface, corresponding to a larger graphitic inclusions previously described in the optical microscope image. In this experiment, the peak stress is 4.7 GPa and this occurs at image 1. The stress rate, $\dot{\sigma}$, is 210 MPa/μs and this is determined from the slope of the stress-time plot between 10 and 90 % of the peak stress. For reference, the dashed line in the stress-time curve is this linear fit between 10 and 90 % of the peak stress. The corresponding strain rate, $\dot{\epsilon}$, is obtained by dividing the stress rate by the Young's modulus. In this experiment, the strain rate is 480 s^{-1}.

There are no visible features on the imaged surface in images 1 and 2. Cracks have likely formed elsewhere in the sample, and this is why the stress has decreased between images 1 and 2. Image 3, which is approximately 3 μs after peak stress, shows a horizontal axial crack that has propagated partially across the face of the sample (highlighted with arrow). In image 4, approximately 4 μs after peak stress, several additional axial cracks grow across the sample, which causes the stress in the material to collapse further. Also observed in image 4 is an example of a larger graphitic disk that appears to grow an axial crack (highlighted with arrow). On average, these surface-breaking axial cracks appear to propagate at a projected speed of 5.0 ±1.1 km/s for the in-plane direction and 3.2±1.1 km/s for the TT direction. These are obtained by tracking the displacement of the crack tip of the first few axial cracks over a multiple camera frames. Cracks that form and grow beyond 8 μs after peak stress are not considered in the analysis. Crack speeds are likely higher when the material is loaded in the in-plane direction because of the fewer defects in their path as a result of preferred orientations, and the increased strength in that direction (presented later in this subsection). We note that

these cracks are higher in speeds than those reported in Hogan et al. [6], which were 2.0 ±0.3 km/s when the material was loaded in the TT direction. This may be due to higher camera resolution and better specimen surface quality since those experiments, as well as averaging over more experiments.

3.2. Rate-Dependent Uniaxial Compressive Strength

Next, we present a summary of the rate-dependent uniaxial compression strength measurements for the IP (squares) and TT (indicated as dots) directions in Figure 4. In Figure 4a, the uniaxial compressive strength is plotted against strain rate. From the plot, we see that the IP strengths are larger than the TT strength for both strain rates, with the IP values also exhibiting less scatter. The strain-rate dependent strength data is normalized (terms to be presented) and compared against the rate dependent strength model of Kimberley et al. [9] in Figure 4b. The Kimberley et al. [9] model incorporates fundamental physics related to crack initiation, growth, and interaction. The model is sensitive to key microstructural (e.g. defect size) and material parameters (e.g. Young's modulus), and has the form:

$$\frac{\sigma_c}{\sigma_0} = 1 + \left(\frac{\dot{\epsilon}}{\dot{\epsilon}_0}\right)^{2/3}. \tag{1}$$

Here, σ_c is the strain-rate dependent compressive strength and $\dot{\epsilon}$ is the applied strain rate. σ_0 is a characteristic compressive strength term (taken here as the quasi-static compressive strength) which depends on the internal flaw distribution through:

$$\sigma_0 = \alpha \frac{K_{Ic}}{\bar{s}\eta^{1/4}}, \tag{2}$$

where K_{Ic} is the Mode I fracture toughness (Pa $\sqrt{m}$), $\bar{s}$ is the average flaw size (m), and η is the areal flaw density (m^{-2}). The term α is a dimensionless proportionality constant.

The corresponding characteristic compressive strain rate, $\dot{\epsilon}_0$, is defined as:

$$\dot{\epsilon}_0 = \alpha \frac{v_c K_{Ic} \eta^{1/4}}{\bar{s} E} \tag{3}$$

where v_c is a limiting crack growth speed (m/s), and E is the Young's modulus (Pa). Kimberley et al. [9] have shown that this model captures the behavior of a large number of brittle materials. We compare experimental results from this study with their model in Figure 4b. First, to compare the results of the unconfined compression experiments with this model, values of σ_0 and $\dot{\epsilon}_0$ must be determined. σ_0 is taken here as the average of the quasi-static experimental strength data. $\dot{\epsilon}_0$ is then determined using a least-squares fit for equation 1 with the experimental data. Values for σ_0 and $\dot{\epsilon}_0$ are presented in Table 1 for both loading orientations, and these values are contrasted later in the discussion. In Figure 4b we see that the experimental strength results can be adequately described by the scaling law form. However, the small experimental range of strain rates (up to 400 s^{-1}) in comparison to the characteristic strain rate (>9x10^3 s^{-1} from Table 1), together with the scatter in the data, makes it challenging to test the power law fit of equation 1. Our experimental results are in a relative rate-sensitive domain.

3.3. Dominant Defect Contributing to Failure

We now consider which defects contribute to the uniaxial compressive failure of boron carbide by examining SEM images of fracture surfaces from a dynamic experiment in Figure 5. Initially, we investigate a fracture surface for the TT loading orientation in Figure 5a to identify the mode of fracture. The loading orientation is denoted. The surface in Figure 5a is relatively smooth, suggesting that transgranular fracture is the dominant failure mode, and it contains relatively few debris. We examine the highlighted region on the surface in a higher magnification image in Figure 5b. Highlighted

in Figure 5b are graphitic disks emerging from the fracture surface. New fracture surfaces are also observed to be growing perpendicular to both ends of one of elongated graphitic disks, suggesting these particles may serve as fracture initiation sites. These features are similar in character to that expected from the wing-crack mechanism that is used to explain the compressive failure of brittle materials [19, 20].

Next, we examine fracture surfaces from a fragment from dynamic experiment performed in the IP orientation in Figure 5c and d. The SEM image in Figure 5c is taken at a lower magnification. The compressive loading direction is also indicated. The surface is again transgranular in nature, and is generally not as smooth as the TT loading orientation. A higher magnification image of the highlighted area in Figure 5c is shown in Figure 5d. As before, graphitic disks are observed protruding from the fracture surface, with some evidence of initiation from these defects as indicated by the scabs features. Wing-crack growth is not as apparent, and this is likely because of the orientation of the graphitic disks.

3.4. Defect Statistics: Size and Orientation

Now that the graphitic disks have been identified as sites for fracture initiation, statistics (i.e., size and orientation) of these defects are considered. Quantification of defects has not been considered in great detail in past studies investigating strength and failure of boron carbide (e.g., [21–24]), or many other advanced ceramics. It is believed that improved interpretations of failure mechanisms and strength measurements can be obtained when flaw populations are more carefully considered, especially considering that ”boron carbide” materials vary from study to study and year to year. An optical microscope image of the microstructure taken in a plane normal to the IP direction at a 100× magnification is shown in Figure 6. We use image processing tools in Matlab [25]

to convert the images to monochrome by thresh-holding. A sample monochrome image is also shown in Figure 6. Measurements of the defects (now appearing as white), such as the major axis dimension ($2s$) [1], orientation [2] (θ), and areal defect density (#/m^2) are then determined. This image processing routine is done for a total of 350 images at a magnification of 100×. We also match the pixel values of the white features to those values in the original image, and this allows us to get an average pixel color intensity. We associate high greyscale intensity with the AlN and BN phases.

The methods outlined in Figure 6 are used to compute the defect statistics for the aluminum nitride and boron nitride, the smaller graphitic defects/pores, and the larger graphitic disks. These methods were developed in the paper by Hogan et al. [6], and preliminary analysis was applied in Farbaniec et al. [20]. In this current paper we only present measurements for the graphitic disks, which we considered as those carbonaceous defects that have aspect ratios > 2.5. Smaller than 2.5 are considered as the smaller graphitic defects, and these form their individual subset. The brighter phases are removed from the total flaw population based on their grayscale color intensity. Using these conditions, we are able to compute an average areal defect density (η: #/m^2) of *just* the graphitic disk subset. Areal defect densities are computed by counting the total number of defects measured for a given image and dividing it by the image area. The average areal defect density for *all* defects (smaller and larger graphitic defects, and AlN and BN) is $1.06\pm0.28\times10^{10}$ #/m^2. The areal defect density for *just* the graphitic disks in the IP images (where the disks appear as ellipsoids) is $1.41\pm0.58\times10^{9}$ #/m^2, and for TT direction (where the disks appear more circular) is $4.16\pm0.65\times10^{8}$ #/m^2. One

[1]The major axis dimension is taken as the longest spanning dimension of the white features in Figure 1d.

[2]The orientation of a white feature is taken in the direction of the major axis dimension. A zero degree orientation is horizontal in the optical image and all orientation angles vary between ±90°.

can see how there appears to be less defects on the TT face (Figure 1). As a convention, we associate the loading direction with the defects that are encountered in that direction, and thus define η_{TT}=1.41±0.58×10^9 #/m^2 and η_{IP}=4.16±0.65×10^8 #/m^2.

Next, the statistical distributions of graphitic disk size and orientation are considered in the probability plots of Figures 7a and b. Histogram forms of this data have been previously reported in Farbaniec et al. [20], although that information is not in as readily useable. The probability plot is used for assessing whether or not an empirical data set, here it is the defect size/orientation, follows a given reference distribution (e.g., lognormal, normal). In a probability plot, the y-axis is scaled accordingly to make the selected reference distribution appear as a straight line. Differences between the reference line and the data set indicate a lack of fit. Mathematically: consider an ordered set of data:

$$\bar{x}_{(1)}, \bar{x}_{(2)}, ...\bar{x}_{(m)} \tag{4}$$

with probability distribution $g(\bar{x})$. The cumulative distribution function, $G(x)$, is given as:

$$G(x) = \int_0^x g(\bar{x})d\bar{x} \tag{5}$$

where $G(x)$ ranges between 0 and 1. From this, we are then able to compute percentile values of $G(x)$. For example, then 35th percentile of the data set occurs when $G(x)$=0.35. If $F(y)$ is the cumulative distribution of a reference distribution $f(\bar{y})$ (e.g., $f(\bar{y})$ is log-normal or normal), then we are able to contrast expected percentiles for both the data ($G(x)$) and reference cumulative distributions ($F(y)$). If the experimental data trends with the reference distribution then the two overlay eachother on the probability plot.

The distribution of graphitic disk size (s) is plotted as a probability plot in Figure 7a. Note here that the total length of the disk is 2s, but we present the half-size as this is

the convention for computational modelling [8]. In Figure 7a, the sizes are compared against a lognormal reference distribution in the form:

$$f(x)_{\ell og} = \frac{1}{x\sigma_{\ell og}\sqrt{2\pi}} e^{-(\log(x)-\mu_{\ell og})^2/2\sigma^2_{\ell og}} \tag{6}$$

where $\mu_{\ell og}$ and $\sigma_{\ell og}$ are the mean and standard deviation of the data's logarithm, and these are obtained from a least squares fit of the data. The lognormal distribution fit the data the best when compared to others (e.g., Weibull, normal). From Figure 7a, we see that the sizes are adequately described using a lognormal distribution when $\mu_{\ell og}$=1.30±0.02 μm and $\sigma_{\ell og}$=0.53±0.02 μm. Note that the minimum size of the graphitic disks is 0.40 μm, the maximum is 40 μm, and the mean is s=4.22 ± 2.54 μm. These are obtained for the set of images taken at 100 x magnification. Also note that we have also observed a few larger carbonaceous defects. They were approximately 200 μm in size on fracture surfaces, but these were not captured in the set of images used to compute these defect statistics. While these defects *may* be nucleated during compressive loading, especially for quasi-static loading, our current size distributions would indicate that all defects with $2s$>100 μm represent much less than 1 % of the total graphitic disk population statistics. Thus, we feel as though our data is complete. The mean size of the aluminum nitride is 0.64 ± 0.53 μm, and for the faceted graphitic particles and/or pores the mean is 2.10 ± 1.26 μm.

Orientation distributions for the graphitic disks as viewed on IP face are considered next in Figure 7b. Again, a defect will have an orientation of 0° if its major axis is aligned parallel with the horizontal in an optical microscope image. A normal distribution in the form of:

$$f_n(x) = \frac{1}{\sigma_n\sqrt{2\pi}} e^{-(x-\mu_n)^2/2\sigma^2_n} \tag{7}$$

is used as the reference distribution in Figure 7b. Other distributions did not fit the data. Here, μ_n is the mean and σ_n is the standard deviation of the orientation data set. If the measured orientation distributions follow the hashed line then it has a normal distribution with a mean of $0\pm1^\circ$ and a standard deviation of $20\pm1^\circ$. As can be seen, the graphitic disks are well described by the normal distribution for orientations of $\pm20^\circ$, reaffirming that most of the disks lay perpendicular to the hot-pressed direction. Although not shown, the disks have no preferred orientation in the TT direction because they are near-circular (Figure 1b). Lastly, the orientation distributions are also random for the aluminum nitride and the facetted graphitic features because they are close to spherical.

4. Summary and Discussion

In this final section, defect quantification, strength measurements and failure characterization are bridged with the scaling law by Kimberley et al. [9] to better understand our experimental results, as well as results by Sano et al. [14] who investigated the dynamic strength of a pressureless sintered boron carbide.

4.1. Defects and Failure

The wing-crack mechanism is typically used to describe the compressive failure of brittle materials [19]. In this mechanism, tension cracks are nucleated at the tip of individual inclined flaws (modelled as slit flaws) and grow to maximize the mode I stress intensity factor [26]. In our hot-pressed boron carbide, it appears that graphitic disks act to nucleate the so-called wing-cracks (Figure 5b) because of their relative size, orientation, and aspect ratio. Initiation from the graphitic disks is believed to be a result of the relative ease of sliding of parallel graphitic surfaces due to a relatively low coefficient of friction. When the material is loaded in the TT direction, the wing-crack-like failure

is apparent (Figure 5b). This is described further in Farbaniec et al. [20]. When the material is loaded in the in-plane direction, failure is still believed to be initiated from the graphitic disks, although there is effectively a smaller number of defects in that plane (compare images Figure 1a and b). The fracture mode is predominantly transgranular in this boron carbide material, as is suggested by the relatively smooth surfaces for both loading orientations.

In order to better understand strength and failure, as well as to more closely characterize the material, defect statistics were examined for the graphitic disk population. The graphitic disks represent less than 15 % of the total flaw population and have preferred orientations in the horizontal of the in-plane direction. The preferred orientation is likely a result of the pressure-aided densification process used to produce the material. Graphitic disk size distributions (s) were found to be well described by a lognormal distribution ($\mu_{\ell og}$= 1.30±0.02 μm, $\sigma_{\ell og}$=0.53±0.02 μm). Power-law functions are commonly used to describe flaw size distributions [13, 27–29], but do not describe this boron carbide flaw size distributions data well. In their study on carbon inclusions in silicon carbide, Bakas et al. [2] used a Jayatilaka and Trustrum [30] probability distribution function to fit histograms. The choice of function by Bakas et al. [2] did not describe the larger tail of the distribution well for their data and fits of histograms are biased towards bin centre locations. Adequately defining larger flaw families is important because of the relative importance of the larger defects on brittle failure, especially at quasi-static rates.

4.2. Rate-Dependent Strength

As the compressive loading proceeds, new cracks will be activated, existing cracks will continue to grow and the material will continue to absorb strain energy (and it

will also contain additional kinetic energy under dynamic loading because of release waves), until a critical rate of damage is achieved. At this point the peak stress (i.e., compressive strength) is reached, the material begins to lose its load-carrying capacity and massive failure ensues. During failure, the damage rate increases rapidly as more cracks are nucleated, crack coalescence occurs, and structuralization follows (i.e., the onset of fragmentation). The rate-dependent strength of this hot-pressed boron carbide was explored for two orientations, one with the loading direction along the hot-pressing direction (TT), and the other with the loading direction in the plane of the plate (IP) (Figure 1). The scaling law proposed by Kimberley et al. [9] (equation 1) was found to adequately describe the experimental data with $\sigma_{0\ TT}$= 3.26 GPa and $\dot{\epsilon}_{0\ TT}$= 9×10^3 s^{-1} for the through-thickness loading orientation, and $\sigma_{0\ IP}$= 4.23 GPa and $\dot{\epsilon}_{0\ IP}$= 3×10^4 s^{-1} for the in-plane loading orientation. In what follows, we explore the applicability of the functional forms of the Kimberley et al. [9] characteristic terms to predict values for the characteristic strength and strain rate, and then explore why there are differences in strength and characteristic strain rates for both loading orientation.

4.2.1. Applicability of Scaling Relationship with Quantified Defect Population

Our experimental measurements of the characteristic strength (σ_0) and characteristic strain rate ($\dot{\epsilon}_0$) for the through-thickness orientation are compared to the predictions from equations (2) and (3), which are estimated using the flaw statistics ($\bar{s}$ and η) measured in this study. Here the example is taken for the through-thickness orientation because of the similarity of its failure to the wing-crack mechanism [20]. Using σ_0=3.26 GPa (measured), K_{Ic}=2.5 MPa $\sqrt{m}$, η=1.41×10^9 #/m^2 and $\bar{s}$=4.22 μm (both measured here), α is computed from equation (2) as α=1.06, indicating that the model is satisfactory at estimating the quasi-static strength when the defect populations and material

properties are known. The theoretical value of $\dot{\epsilon}_0$ is then estimated as $\dot{\epsilon}_0$=9×10^5 s^{-1} using the measured crack speed of v_c=3,200 m/s and a stiffness of E=430 GPa. This is two orders of magnitude larger than the highest experimental strain rate. Thus the model suggests, based on the flaw statistics, that the strength should be relatively insensitive to strain rates over the experimental range of rates. This is what is observed.

4.2.2. Orientation Effects on Strain-Rate Dependent Strength

In this subsection, the defect measurements are used to explore why the characteristic strength and characteristic strain rate are greater in the in-plane direction than in the through-thickness direction ($\sigma_{0\ IP}$= 4.23 GPa vs. $\sigma_{0\ TT}$= 3.26 GPa, and $\dot{\epsilon}_{0\ IP}$= 3×10^4 s^{-1} vs. $\dot{\epsilon}_{0\ TT}$= 9×10^3 s^{-1}). First, fewer properly orientated defects are available when the material is loaded in the in-plane direction (Figures 1 and 7b), and this allows us to define an expected increase in the quasi-static strength for the in-plane direction based on equation (2) from Kimberley et al. [9] (assuming K_{Ic} and $\bar{s}$ are the same for both orientations):

$$\frac{\sigma_{0\ IP}}{\sigma_{0\ TT}} \propto \frac{\eta_{TT}^{1/4}}{\eta_{IP}^{1/4}} = 1.35 \tag{8}$$

This expected increase based on the defect density compares favorably with the experimentally measured differences in quasi-static strength of $\sigma_{0\ IP}/\sigma_{0\ TT}$=4.23 GPa/3.26 GPa=1.29, suggesting that the decrease in effective flaw density is likely partially responsible for the increase in strength in the through-thickness direction.

Next, we consider the effect of the hot-pressing direction on the characteristic strain rate. Assuming fracture toughness, stiffness and defect size are the same, then the ratio of the theoretically predicted characteristic strain rates according to the scaling law is:

$$\frac{\dot{\epsilon}_{0\ IP}}{\dot{\epsilon}_{0\ TT}} \propto \left(\frac{v_{c\ IP}\,\eta_{IP}}{v_{c\ TT}\,\eta_{TT}}\right) = 1.21 \tag{9}$$

The scaling law would predict that that characteristic strain rate should be higher for the IP direction than the TT direction. This is also noted experimentally, where the IP characteristic strain rate is greater than in the TT direction. Additional differences between the theoretical and experimental predictions are associated with differences in $\bar{s}$, E, and K_c, as well as our inability to truly measure the characteristic strain rate because our experimentally available rates are much lower than those characteristic strain rates.

4.2.3. Strength Comparison with Literature

With the idea that the scaling laws by Kimberley et al. [9] may be used to understand the relationships between experimental strength measurements and the defect population, we now contrast dynamic uniaxial compressive strength measurements from our hot-pressed pressure aided densified (PAD) boron carbide with those from Sano et al. [14] who studied a pressureless sintered (PS) boron carbide (Figure 8). Note that the experiments were performed for similar strain rates (around 400 s^{-1}), except our quasi-static experiments which are noted in Figure 8. Also note that the PS specimen sizes were the same as the PAD specimens, so size effects are not significant here (note that the scaling law does not explicitly account for the effects of size). However, we know from experiments [31] and micro-mechanical models [13] that larger samples tend to be stronger in dynamic loading regimes. This is related to finite crack velocities, and larger samples taking longer to fail in dynamic loading. As a consequence, the applied stress will be greater in the larger sample and the strength will be higher. The opposite is true for quasi-static loading: larger samples have a greater probability of larger defects, and these tend to dominate quasi-static failure [32]. The summary of dynamic strength measurements with standard deviation are plotted in Figure 8, and are listed in Table 2.

Initially, we comment on the smaller standard deviation in the IP orientation than in

TT for our PAD material: In a study by Graham-Brady [13] the effect of the local flaw density on the rate-dependent compressive strength of brittle materials was investigated. Graham-Brady showed that the spatial distribution of defects can affect the standard deviation (or covariance), where the standard deviation of strength is greater when flaws are uniformly dispersed throughout a microstructure than when flaws are clustered together. In our experiments, the defects are more uniformly distributed on the in-plane face. Thus it is expected that experiments performed in the TT loading direction would show the greater standard deviation, and this is what we observe in the small sample set.

Next, we consider the difference of strengths between the PAD results and the PS results. To accomplish this, we show an optical microscope image of the pressureless sintered boron carbide microstructure in Figure 8 (right). This image is used to highlight the greater number of defects in this material (almost 45× more) than in our current hot-pressed material. We compile a table of some relevant *mechanical properties* in Table 2, which includes the material density (ρ), Young's modulus (E), dynamic compressive strength (σ_f) (which we are comparing) and Knoop hardness (H_K). Values for the PS material are taken from the paper by Sano et al. [14]. In addition, a summary of the *microstructure characteristics* for each boron carbide are shown in Table 3, including the average boron carbide grain size (ℓ'), the average defect size ($\bar{s}$), and the areal flaw densities of carbonaceous defects for $s > 0.5\ \mu m$ (η). Here we have performed our own characterization of the PS to get ℓ', $\bar{s}$ and η. Using the values of mechanical properties and microstructure characteristics, we can explore the expected change in dynamic strength between the two boron carbides. First, the expected change in the *quasi-static*

strength between the PAD and the PS material obtained from equation (2) as:

$$\frac{\sigma_{0\ PAD}}{\sigma_{0\ PS}} \propto \frac{\bar{s}_{PS}\ \eta_{PS}^{1/4}}{\bar{s}_{PAD}\ \eta_{PAD}^{1/4}} \tag{10}$$

Note that this assumes that K_{1c} is the same for each material, which is not likely the case. We do not investigate the change in the characteristic strain rate because the PS tests were only performed at one strain rate, and we do not know the value of $\dot{\epsilon}_0$ for the PS material. Values for the estimated theoretical difference in quasi-static strength computed from equation 2 are shown in Table 4. We note that because the characteristic strain rates for these materials are of the order 10^4 s^{-1}, and we are comparing the experimental strength measurements at $\dot{\epsilon}$=400 s^{-1}, then the theoretical differences in dynamic strength are essentially equal to the theoretical differences in quasi-static strength. Comparing results in Table 4, the experimental results show that the experimental strength is on average 1.27× greater for the PAD TT direction than the PS (but not statistically significant), while the theoretical prediction suggests that the PAD should be 1.74× greater than the PS. The discrepancy could be due to a reduced K_{1c} for the PS material, the preferential activation of certain defects, or possibly due to porosity in pressureless sintered ceramic.

The totality of the experimental results highlight the challenges in (1) evaluating statistically significant effects for compressive strength between two materials, and (2) obtaining a near-complete set of measurements for the mechanical properties and defect populations. Simulations are also needed to better explore the competition between these material properties and microstructure characteristics in terms of the dynamic uniaxial compressive strength and the performance of these materials in application.

5. Concluding Remarks

In this study, the effects of the microstructure and hot-pressing orientation on the compressive strength and failure of boron carbide was investigated. Scanning electron and optical microscopy identified the various types of defects in the microstructure: aluminum nitride and boron nitride, spherical graphitic defects and pores, and graphitic disks. Graphitic disks were observed to be promoters of fracture, and we used image processing techniques to determine their size and orientation, and their number density. Measurements of the defect statistics were used to explain the orientation effects on the compressive strength in this hot-pressed boron carbide, as well as to explain differences between this boron carbide and the pressure-less sintered boron carbide investigated by Sano et al. [14]. All together, the measurements and methodologies developed provide guidelines for future improvements of ceramic performance through microstructural design and simulation.

6. Acknowledgments

This research was sponsored by the Army Research Laboratory and was accomplished under Cooperative Agreement Number W911NF-12-2-0022. The views and conclusions contained in this document are those of the authors and should not be interpreted as representing the official policies, either expressed or implied, of the Army Research Laboratory or the U.S. Government. The U.S. Government is authorized to reproduce and distribute reprints for Government purposes notwithstanding any copyright notation herein. Kanak Kuwelkar from Rutgers and Matthew Bratcher from Army Research Laboratories are acknowledged for discussions of the microstructure. Will Wagers, Joe Hajj and Nicole Cade-Ferreira from the Johns Hopkins University are thanked for helping run the experiments.

7. References

[1] H. Wang, K. T. Ramesh, Dynamic strength and fragmentation of hot-pressed silicon carbide under uniaxial compression, Acta Materialia 52 (2) (2004) 355 – 367.

[2] M. Bakas, J. W. McCauley, V. Greenhut, D. Niesz, R. Haber, B. West, Quantitative analysis of inclusion distributions in hot pressed silicon carbide, International Journal of Impact Engineering 50 (2012) 40–48.

[3] G. Hu, K. T. Ramesh, B. Cao, J. W. McCauley, The compressive failure of aluminum nitride considered as a model advanced ceramic, Journal of the Mechanics and Physics of Solids 59 (5) (2011) 1076 – 1093.

[4] J. LaSalvia, Recent progress on the influence of microstructure and mechanical properties on ballistic performance, Ceramic transactions 134 (2002) 557–570.

[5] M. Chen, J. W. McCauley, K. J. Hemker, Shock-induced localized amorphization in boron carbide, Science 299 (5612) (2003) 1563–1566.

[6] J. D. Hogan, L. Farbaniec, M. Shaeffer, K. Ramesh, The effects of microstructure and confinement on the compressive fragmentation of an advanced ceramic, Journal of the American Ceramic Society 98 (3) (2015) 902–912.

[7] M. S. Williams, Modeling of local impact effects on plain and reinforced concrete, ACI Structural Journal 91 (2) (1994) 178–187.

[8] B. Paliwal, K. T. Ramesh, An interacting micro-crack damage model for failure of brittle materials under compression, Journal of the Mechanics and Physics of Solids 56 (3) (2008) 896–923.

[9] J. Kimberley, K. T. Ramesh, N. P. Daphalapurkar, A scaling law for the dynamic strength of brittle solids, Acta Materialia 61 (9) (2013) 3509–3521.

[10] W. W. Chen, A. Rajendran, B. Song, X. Nie, Dynamic fracture of ceramics in armor applications, Journal of the American Ceramic Society 90 (4) (2007) 1005–1018.

[11] B. Paliwal, K. T. Ramesh, J. W. McCauley, M. Chen, Dynamic compressive failure of alon under controlled planar confinement, Journal of the American Ceramic Society 91 (11) (2008) 3619–3629.

[12] G. Hu, J. Liu, L. Graham-Brady, K. T. Ramesh, A 3d mechanistic model for brittle materials containing evolving flaw distributions under dynamic multiaxial loading, Journal of the Mechanics and Physics of Solids 78 (2015) 269–297.

[13] L. Graham-Brady, Statistical characterization of meso-scale uniaxial compressive strength in brittle materials with randomly occurring flaws, International Journal of Solids and Structures 47 (18) (2010) 2398–2413.

[14]

[15] J. Lankford, Compressive strength and microplasticity in polycrystalline alumina, Journal of Materials Science 12 (4) (1977) 791–796.

[16] W. Chen, G. Ravichandran, Static and dynamic compressive behavior of aluminum nitride under moderate confinement, Journal of the American Ceramic Society 79 (3) (1996) 579–584.

[17] G. Subhash, G. Ravichandran, Mechanical behaviour of a hot pressed aluminum

nitride under uniaxial compression, Journal of Materials Science 33 (7) (1998) 1933–1939.

[18] O. Sologub, Y. Michiue, T. Mori, Boron carbide, b13-xc2-y (x= 0.12, y= 0.01), Acta Crystallographica Section E: Structure Reports Online 68 (8) (2012) 67–67.

[19] S. Nemat-Nasser, H. Horii, Compression-induced nonplanar crack extension with application to splitting, exfoliation, and rockburst, Journal of Geophysical Research 87 (B8) (1982) 6805–6821.

[20] L. Farbaniec, J. Hogan, K. Ramesh, Micromechanisms associated with the dynamic compressive failure of hot-pressed boron carbide, Scripta Materialia 106 (2015) 52 – 56.

[21] C. Anderson, S. Chocron, K. A. Dannemann, A. E. Nicholls, Testing boron carbide under triaxial compression, in: Proceedings of the Conference of the American Physical Society Topical Group on Shock Compression of Condensed Matter, Vol. 1426, AIP Publishing, 2012, pp. 88–91.

[22] N. Bourne, Shock–induced brittle failure of boron carbide, Proceedings of the Royal Society of London. Series A: Mathematical, Physical and Engineering Sciences 458 (2024) (2002) 1999–2006.

[23] G. R. Johnson, T. J. Holmquist, Response of boron carbide subjected to large strains, high strain rates, and high pressures, Journal of Applied Physics 85 (12) (1999) 8060–8073.

[24] S. Hayun, V. Paris, M. Dariel, N. Frage, E. Zaretzky, Static and dynamic mechani-

cal properties of boron carbide processed by spark plasma sintering, Journal of the European Ceramic Society 29 (16) (2009) 3395–3400.

[25] Simulink, 2013 Matlab User Manual.

[26] G. Ravichandran, G. Subhash, A micromechanical model for high strain rate behavior of ceramics, International Journal of Solids and Structures 32 (1718) (1995) 2627 – 2646.

[27] K. R. Housen, K. A. Holsapple, Scale effects in strength-dominated collisions of rocky asteroids, Icarus 142 (1) (1999) 21–33.

[28] H. Abe, M. Naito, T. Hotta, N. Shinohara, K. Uematsu, Flaw size distribution in high-quality alumina, Journal of the American Ceramic Society 86 (6) (2003) 1019–1021.

[29] P. Warren, Fracture of brittle materials: effects of test method and threshold stress on the weibull modulus, Journal of the European Ceramic Society 21 (3) (2001) 335 – 342.

[30] A. S. Jayatilaka, K. Trustrum, Statistical approach to brittle fracture, Journal of Materials Science 12 (7) (1977) 1426–1430.

[31] Q. Qian, C. Qi, M. Wang, Dynamic strength of rocks and physical nature of rock strength, J Rock Mech Geotech Eng 1 (1) (2009) 1–10.

[32] K. R. Housen, K. A. Holsapple, Scale effects in strength-dominated collisions of rocky asteroids, Icarus 142 (1) (1999) 21 – 33. doi:http://dx.doi.org/10.1006/icar.1999.6206.

Table 1: Estimates for the characteristic stress (σ_0) and the characteristic strain-rate ($\dot{\epsilon}_0$), that provide the best fit of the experimental data to the strength model. In-plane loading orientation: IP, through thickness loading orientation: TT.

Loading Orientation	σ_0 (GPa)	$\dot{\epsilon}_0$ (s^{-1})
IP	4.23	3×10^4
TT	3.26	9×10^3

Table 2: Mechanical properties for our hot-pressed pressure aided densified material (PAD) and a pressureless sintered (PS) boron carbide, including material density (ρ), Young's modulus (E), the compressive strength (σ_f) at 400 s^{-1} (unless indicated). QS: quasi-static ($\sim 10^{-4}$ s^{-1}), IP: in-plane loading orientation and TT: through-thickness loading orientation.

Material	ρ (kg/m^3)	E (GPa)	σ_f at 400 s^{-1} (GPa)	H_K (GPa)
PAD	2,510	430	QS: 2.98 ± 0.60 (TT) and 4.23 ± 0.29 (IP) at Dyn: 3.70 ± 0.30 (TT) and 4.47 ± 0.18 (IP)	20.5±1.4
PS	2,460	425	3.34 ± 0.30	19.8±1.2

Table 3: Microstructure characteristics for our hot-pressed pressure aided densified material (PAD) and a pressureless sintered (PS boron carbide, including: ℓ': average boron carbide grain size, $\bar{s}$: average defect size, and η: areal defect density ($\#/m^2$) for s>0.5 μm.

Material	ℓ' (μm)	$\bar{s}$ (μm)	η:s>0.5 μm ($\#/m^2$)
PAD	16.0 ± 2.1	4.22 ± 2.54	$1.41\pm0.58\times10^9$
PS	2.1 ± 0.3	2.83 ± 2.57	$6.44 \pm 0.46 \times10^{10}$

Table 4: Comparison of theoretical and measured changes in strength between PAD and the PS boron carbide materials. σ_0: characteristic strength, and σ_f: compressive strength at 400 s^{-1}, PAD: pressure-aided densificated, and PS: pressure-less sintered.

$\sigma_{0\ PAD}/\sigma_{0\ PS}$ (theoretical)	$\sigma_{f\ PAD}/\sigma_{f\ PS}$ (experimental)
1.74	1.27

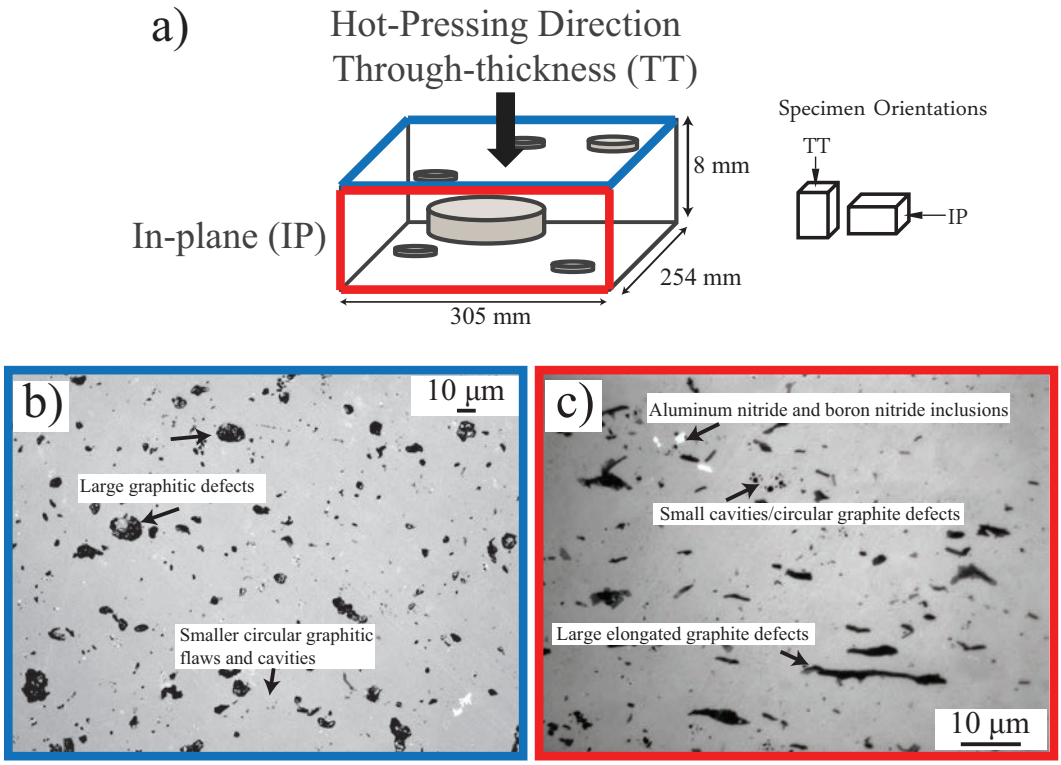

Fig. 1: (a) Conceptualized as-received tile of the hot-pressed boron carbide plate with through-thickness (TT) (in the hot-pressing direction) and in-plane directions (IP) labelled. Optical microscope images of the boron carbide microstructure in the (b) through-thickness (at 10× magnification) and (c) in-plane direction (100× magnification) with the various types of inclusions and defects.

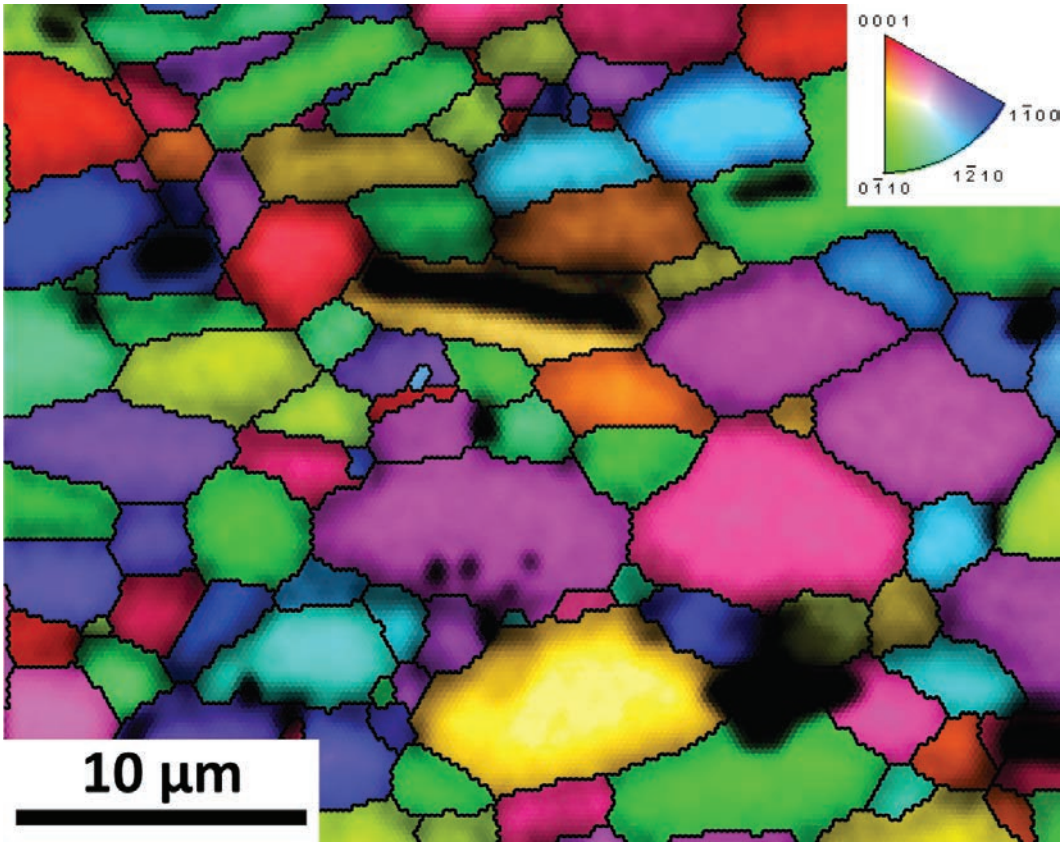

Fig. 2: Combined inverse pole figure (IPF), image quality (IQ) and grain-boundary maps of hot-pressed boron carbide obtained with electron back-scatter diffraction analysis. Dark regions correspond to inclusions and defects present in the microstructure.

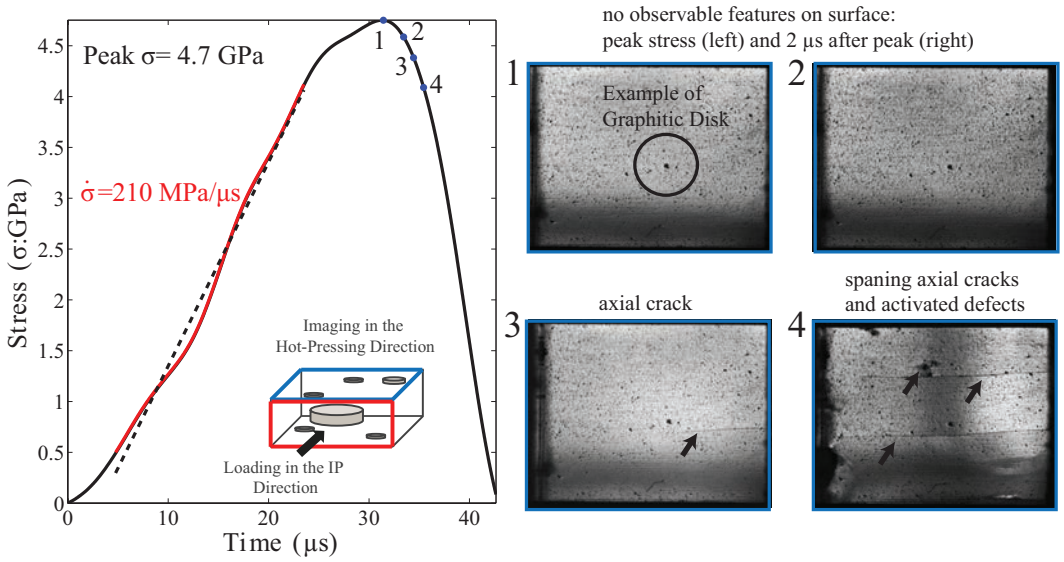

Fig. 3: Stress-time history of dynamic uniaxial compression of boron carbide with time-resolved high-speed video images showing mesoscale failure mechanisms. The loading orientation and the imaging face is shown as an inset. The black dashed line in the stress-time plot is the linear fit of 10 and 90 % of the peak stress and this corresponds to the stress rate $\dot{\sigma}$=210 MPa μ/s.

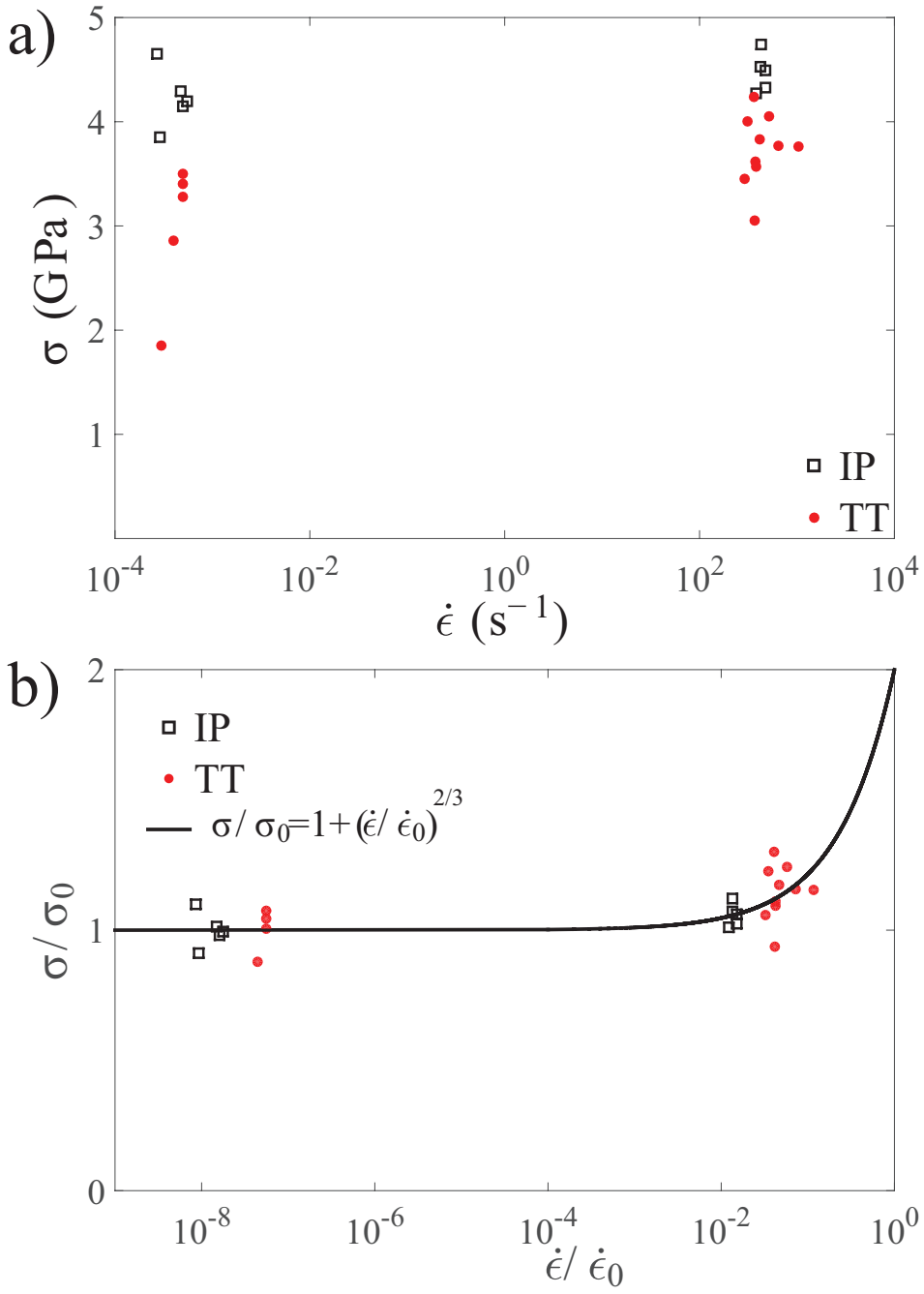

Fig. 4: (a) Uniaxial compressive strength plotted against strain rate for in-plane and through-thickness directions. (b) Normalized uniaxial compressive strength data for in-plane and through-thickness directions for hot-pressed boron carbide samples compared with the strength scaling model of Kimberley et al. [9]. Each orientation is normalized by their respective characteristic strength and characteristic strain rate shown in Table 1.

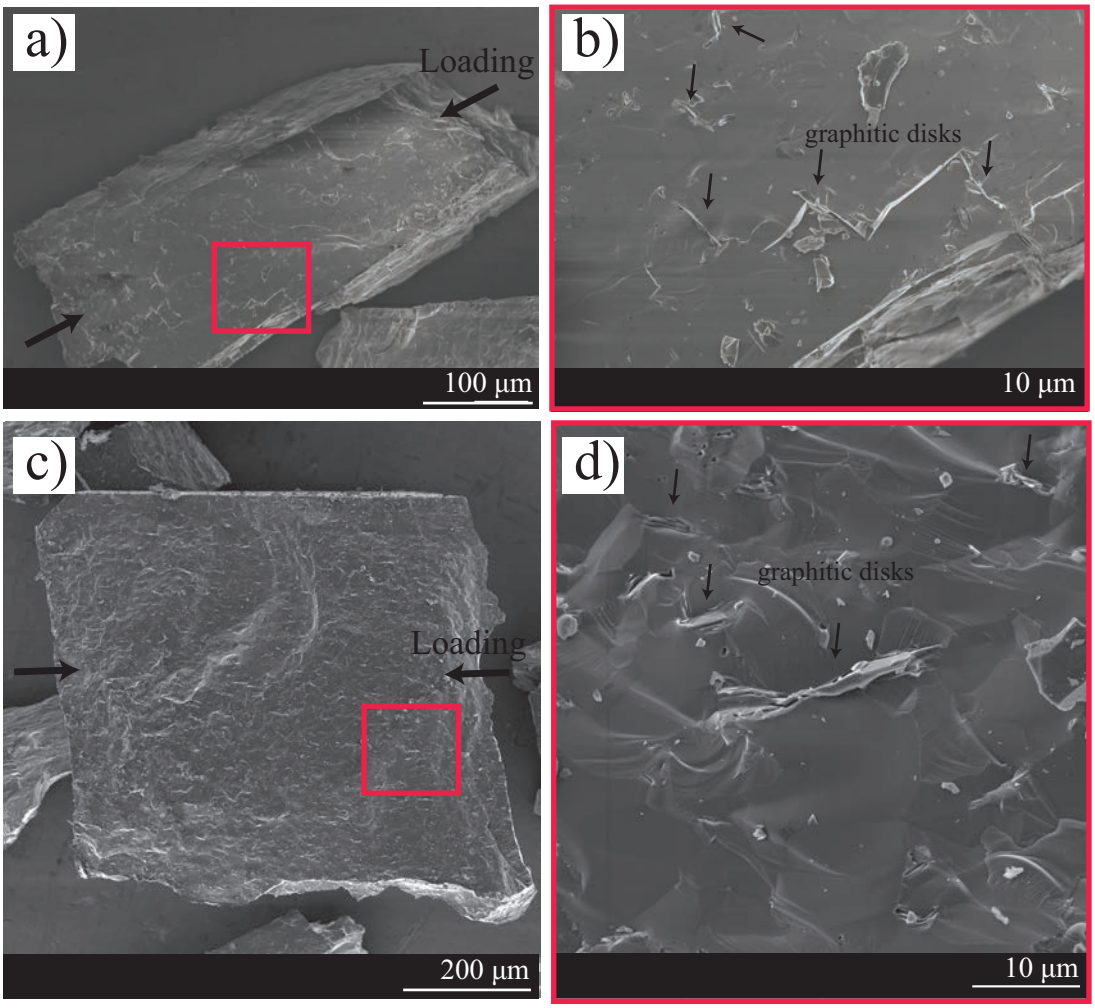

Fig. 5: SEM images for through-thickness loading orientation: (a) blocky fragment with a relatively smooth fracture surface, suggesting transgranular fracture, and (b) fracture surface highlighting fracture initiation from the graphitic disks. IP loading orientation: (c) larger blocky fragment with surfaces show transgranular fracture, and (d) magnified image showing fracture intersecting the graphitic disk on the surface surface. The compressive loading directions are noted in (a) and (c).

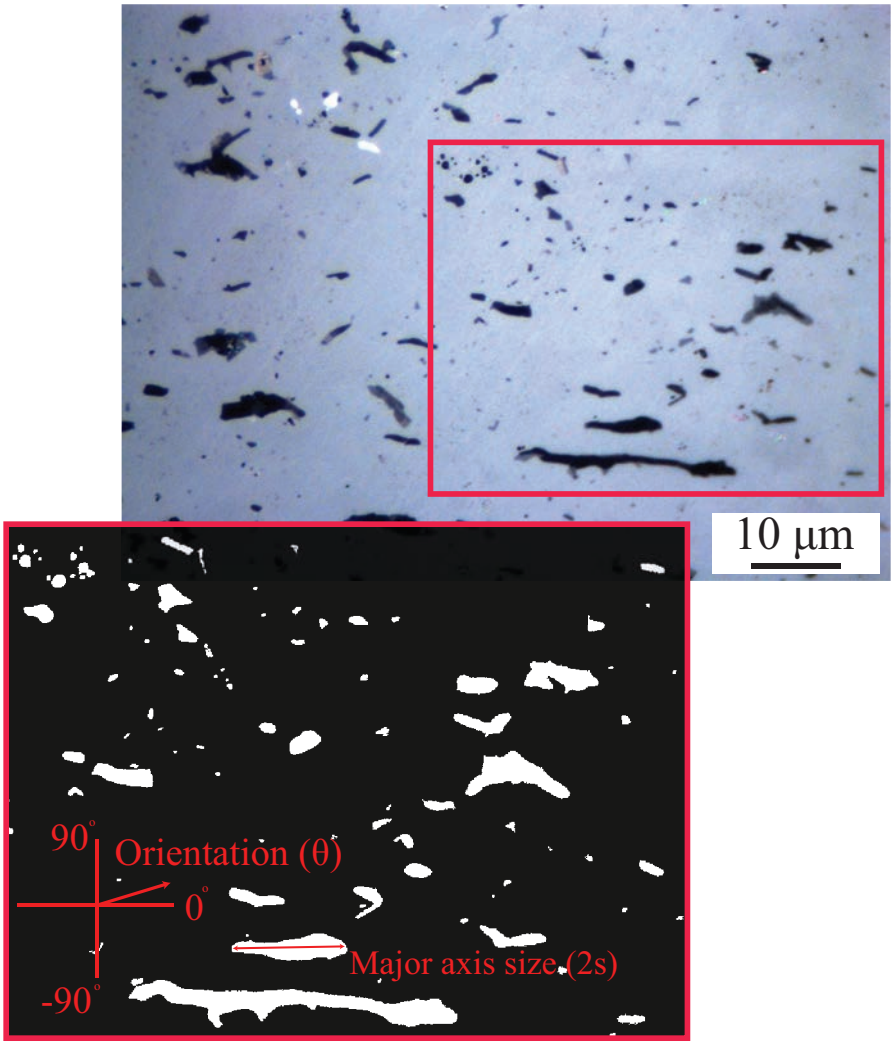

Fig. 6: Optical microscope image with inset of converted monochrome image obtained through image processing that is used to determine the defect major axis size ($2s$), which is the longest spanning dimension of the white feature, and orientation (θ), which is defined as the direction of the major axis dimension.

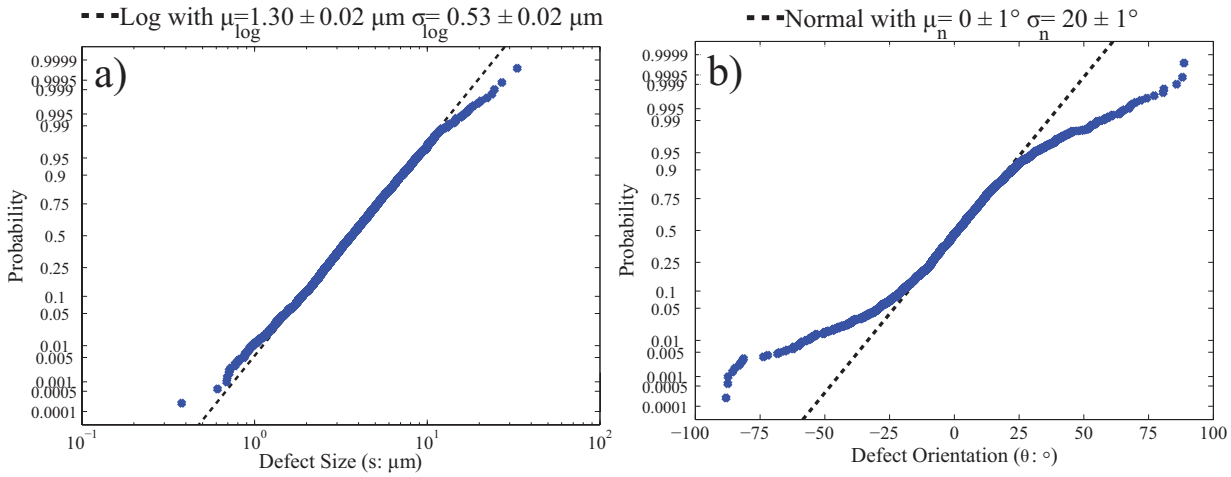

Fig. 7: (a) Probability plot of graphitic size with lognormal reference curve and fits (hashed-lined: $\mu_{\ell og}$= 1.30±0.02 μm, $\sigma_{\ell og}$=0.53±0.02 μm). (b) Probability plot of graphitic disks orientations (as viewed in the in-plane direction) with normal reference curve and fits (hashed-lined: μ_n= 0±1°, σ_n= 20±1°).

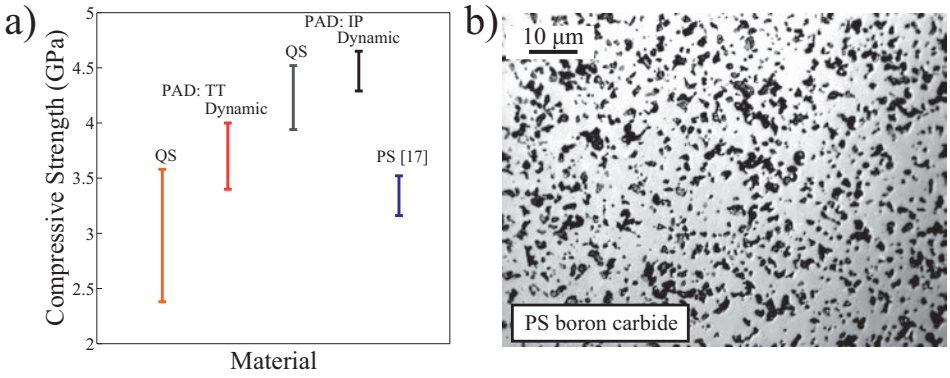

Fig. 8: (a) A comparison of strength measurements between this study and Sano et al. [14]. PAD: pressure-aided densification (hot-pressed), and PS: pressure-less sintered. (b) Optical microscope image of the PS material microstructure used in Sano et al. [14].

***Graphical Abstract**

Stress-time history (left) with high-speed image (right) showing axial cracking intersecting large graphitic defect in the hot-pressed boron carbide.

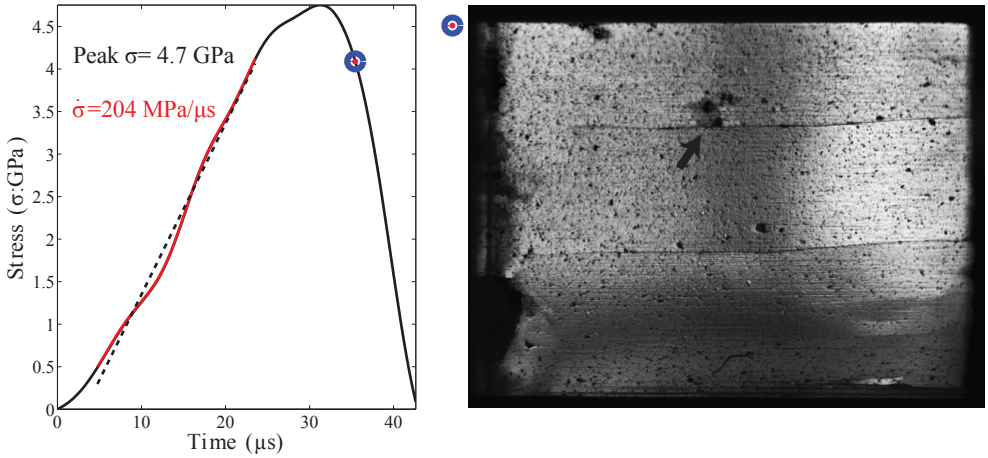

SEM image confirming graphitic defects site for fracture initiation (left).
Image processing techniques are used to determine their size and number (right).

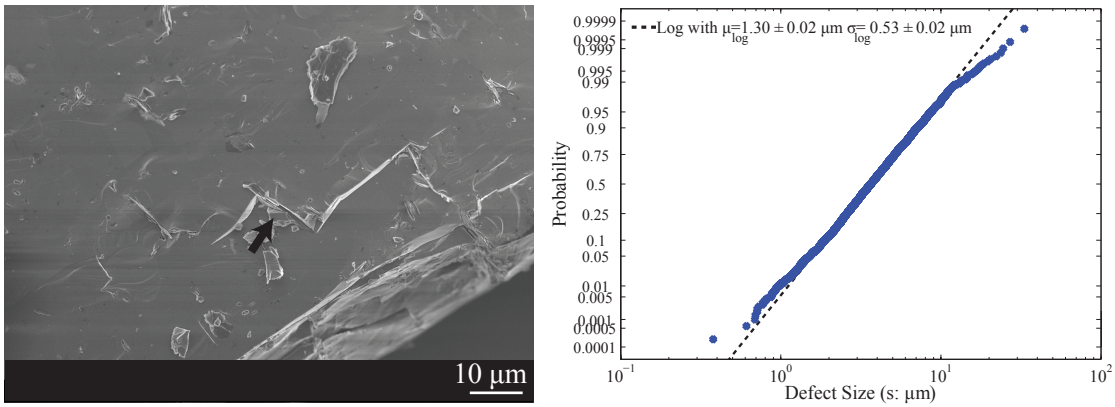

Using measured defect populations, we explore experimental measurements of rate-dependent compressive strengths using the Kimberley et al. 2013 (Acta Materiala) scaling law.